This is a repository copy of *When do fractured media become seismically anisotropic? Some implications on quantifying fracture properties*.

White Rose Research Online URL for this paper:
http://eprints.whiterose.ac.uk/97216/

Version: Accepted Version

Article:

When do fractured media become seismically anisotropic? Some implications on quantifying fracture properties

Yousef, B.M. & Angus, D.A.

School of Earth & Environment, University of Leeds, Leeds, LS2 9JT, UK

Corresponding author: Doug Angus, d.angus@leeds.ac.uk

Abstract

Fractures are pervasive features within the Earth's crust and have a significant influence on the multi-physical response of the subsurface. The presence of coherent fracture sets often leads to observable seismic anisotropy enabling seismic techniques to remotely locate and characterise fracture systems. In this study, we confirm the general scale-dependence of seismic anisotropy and provide new results specific to shear-wave splitting (SWS). We find that SWS develops under conditions when the ratio of wavelength to fracture size (λ_S/d) is greater than 3, where Rayleigh scattering from coherent fractures leads to an effective anisotropy such that effective medium model (EMM) theory is qualitatively valid. When $1 < \lambda_S/d < 3$ there is a transition from Rayleigh to Mie scattering, where no effective anisotropy develops and hence the SWS measurements are unstable. When $\lambda_S/d < 1$ we observe geometric scattering and begin to see behaviour similar to transverse isotropy. We find that seismic anisotropy is more sensitive to fracture density than fracture compliance ratio. More importantly, we observe that the transition from scattering to an effective anisotropic regime occurs over a propagation distance between 1 to 2 wavelengths depending on the fracture density and compliance ratio. The existence of a transition zone means that inversion of seismic anisotropy parameters based on EMM will be fundamentally biased. More importantly, we observe that linear slip EMM commonly used in inverting fracture properties is inconsistent with our results and leads to errors of approximately 400% in fracture spacing (equivalent to fracture density) and 60% in fracture compliance. Although EMM representations can yield reliable estimates of fracture orientation and spatial location, our results show that EMM representations will systematically fail in providing quantitatively accurate estimates of other physical fracture properties, such as fracture density and compliance. Thus more robust and accurate quantitative estimates of *in situ* fracture properties will require improvements to effective medium models as well as the incorporation of full-waveform inversion techniques.

Keywords: explicit fractures, finite-difference, full-waveform synthetics, scattering, seismic anisotropy, shear-wave splitting

1. Introduction

The Earth's crust is brittle down to approximately 20 km depth (e.g., Rolandone et al., 2002) and, as such, fractures are expected and observed to be pervasive features within these depths (e.g., Liu & Martinez, 2012). Fractures range in size over several orders of magnitude, from large-scale faults (100 kms) observed on the Earth's surface down to micro-cracks (μm) observed

in core samples. Since fractures are ubiquitous features and vary in size over several orders of magnitude (e.g., Narr, 2006), they play a critical role in the multi-physical response of Earth materials. Fractures control the behaviour of geo-mechanical deformation influencing the evolution of the stress and strain fields (e.g., Segall, 2010; Cornet, 2015) and act as conduits for fluid-flow in porous crustal rocks (e.g., Franciss, 2010). For geo-industrial applications, such as hydrocarbon exploration (e.g., Herwanger & Koutsabeloulis, 2011), geothermal energy (e.g., Gaucher et al., 2015), geo-sequestration of CO_2 (e.g., Cook, 2014) and deep geological storage of nuclear waste (e.g., Jaeger et al., 2007), the mechanical and fluid-flow properties of fractures is of critical importance. For instance, fractures have a significant influence on the integrity of boreholes and the sealing capacity of the reservoir overburden and their ability for maintaining barriers between potable water and hydrocarbon, CO_2 or radioactive waste. For non-geo-industrial applications, such as monitoring volcanoes, landslides and earthquakes, fractures have a significant influence on the stability of the rock mass and so have important implications on geo-hazard assessment (e.g., Hamlyn et al., 2014).

Often it is assumed that fractures are critically stressed (e.g., Crampin, 2005; Zoback & Gorelick, 2012) and/or that movement along fractures increases permeability (e.g., Barton, 2007). The assumption of increased permeability due to fault movement is debatable as some studies have observed that fault movement may occur without significantly increasing permeability when rocks have high porosity and are normally consolidated (e.g., Fisher et al., 2003). Thus, even though we have known for sometime that fractures are prevalent within the crust, it is apparent from such studies that the *in situ* physical properties of fractures still are not well constrained. Hence geophysical imaging of fractures and extracting fracture properties is becoming increasingly important, especially being able to quantify the nature of the fracture infill to assess flow potential for leakage assessment or frictional shear-strength for hazard assessment.

Fractures alter the mechanical and fluid flow properties of rocks and so seismic measurements will be sensitive to the presence of *in situ* fractures (e.g., Liu & Martinez, 2012). Furthermore, since fractures and joints tend to cluster in coherent regions with a directional dependence of reduced stiffness (or increased compliance) associated with stress and strain concentrations within a rock mass, observable seismic anisotropy is often a diagnostic phenomenon (e.g., Crampin, 1981). In other words, the strength of the reduced fracture stiffness is quantified in terms of fracture normal and tangential compliance, where the magnitude of compliance controls the strength of the seismic anisotropy (e.g., an increase in compliance leads to an increase in anisotropy). Seismic anisotropy refers to directional variations in seismic velocities, which in crustal rock can be due to intrinsic anisotropy from preferred orientation of minerals (e.g., Babuska & Cara, 1991), sedimentary layering (e.g., Babuska & Cara, 1991), coherent alignment of sub-seismic scale fractures (e.g., Crampin, 1981; Nakagawa et al., 2003; Baird et al., 2013) and the influence of non-hydrostatic changes in the stress field on micro-cracks and grain boundaries (e.g., Verdon et al., 2008).

There are several seismic methods that can be used to infer fracture properties in the subsurface; the most common being anisotropic velocity model analysis (e.g., Jones, 2010), amplitude versus offset and azimuth (AVOA) analysis (e.g., Liu & Martinez, 2012) and shear-wave splitting (SWS) analysis (e.g., Savage, 1999). These approaches can infer orientation and density of fractures as well as monitor temporal and spatial variations in fracture properties (e.g., Teanby et al., 2004a). For example, SWS analyses applied to teleseismic (Hammond et al., 2010), regional seismicity (e.g., Keir et al., 2011) and microseismicity (e.g., Verdon & Wüstefeld, 2013) data have been used to estimate fracture properties, such as width of fracture (or melt) zones as well as orientation, density and fracture compliance. These methods have shown great promise in

2

qualitatively characterising a range of fracture properties and potentially to quantify the physical properties and distribution of natural and induced fracture systems. Distinguishing between the various sources of seismic anisotropy as well as seismic heterogeneity is often not a simple task, and interpretation can be complicated further by frequency-dependent anisotropy (e.g., Yi et al., 1997; Maultzsch et al., 2003; Baird et al., 2013).

To estimate or invert for the fracture properties a rock physics model is required to map the measured seismic anisotropy attributes (e.g., SWS) to the physical fracture properties. In general there are two approaches to model fractured rock: effective medium models (EMM) and discrete fracture models (DFM). EMM is the most common approach for modelling the seismic behaviour of fractured rock (e.g., Hall, 2000; Baird et al., 2013). EMM is a volumetric approach and models the fractured rock as an effective elastic medium, such that the elastic constants are anisotropic (e.g., O'Connell & Budiansky, 1974; Crampin, 1981; Sayers & Kachanov, 1991). While much has been achieved with these methods, there are limitations such as the applicable frequency range, the types of fracture properties which can be studied, and non-uniform influences for example due to stress-field (e.g. Hildyard, 2007). The main restriction for EMM is that it is valid only when the dominant seismic wavelength of the propagating wave is much greater than the heterogeneity induced by the fractures; this is referred to as the long wavelength approximation (LWA). Furthermore, EMM assumes the rock mass is 'instantaneously' anisotropic and so does not allow for the transition from a scattering regime to an effective anisotropy regime.

The alternative approach is to model fracture networks as discrete elements that can encapsulate individual fracture behaviour (e.g. Hildyard, 2007). DFM allows us to reduce many assumptions about the model and enables the solution to simulate the interaction of seismic waves with fractures systems more correctly. DFM models can capture the influence of the stress state, as well as specific fracture properties such as fracture size, fill and compliance. Furthermore, DFM is not restricted by the LWA and allows the dominant seismic wavelength to be greater, less than or equal to the fracture size, allowing the characterisation of low-frequency behaviour (i.e., LWA regime) and high-frequency behaviour (i.e., ray theoretical limit). However, it is generally difficult to determine the spatial geometry of fracture systems deterministically and often the computational costs associated with modelling discrete fractures can be a barrier.

Figure 1 illustrates some of the uncertainties in inferring fracture properties from seismic anisotropy. Figure 1(a) shows two ray paths (P_1 and P_2) of equal length propagating through a fracture zone consisting of discrete fractures. The ray path perpendicular to fracture strike (P_1) will experience a longer travel time than the ray path traveling along strike (P_2) due to the presence of the seismic discontinuities (e.g., Babuska & Cara, 1991). This leads to an effective velocity anisotropy with seismic velocity being greater along strike than perpendicular to strike. In Figure 1(b) we include an elliptical velocity anomaly that can lead to either (i) a perceived greater seismic velocity anisotropy (if the anomaly is a high-velocity ellipse) or a perceived smaller seismic velocity anomaly or isotropy (if the anomaly is a low-velocity ellipse). This illustrates the inherent ambiguity of traveltime anisotropic velocity analysis. In Figure 1(c) we apply the standard approach to modelling fractures by introducing a homogeneous representation of the discrete fractures with an elastically anisotropic zone based on an effective rock physics model of the fracture zone (e.g., Liu & Martinez, 2012). Since seismic anisotropy evolves as the wave propagates through a discrete fracture system, there is a region within the fracture volume where the interaction of the wave with the fractures transitions from a scattering regime to an effectively anisotropic regime. This is depicted in Figure 1(d) where we introduce a 'buffer' zone around a smaller effective homogeneous fracture zone.

Under what conditions do fractured media become seismically anisotropic? How do we de-
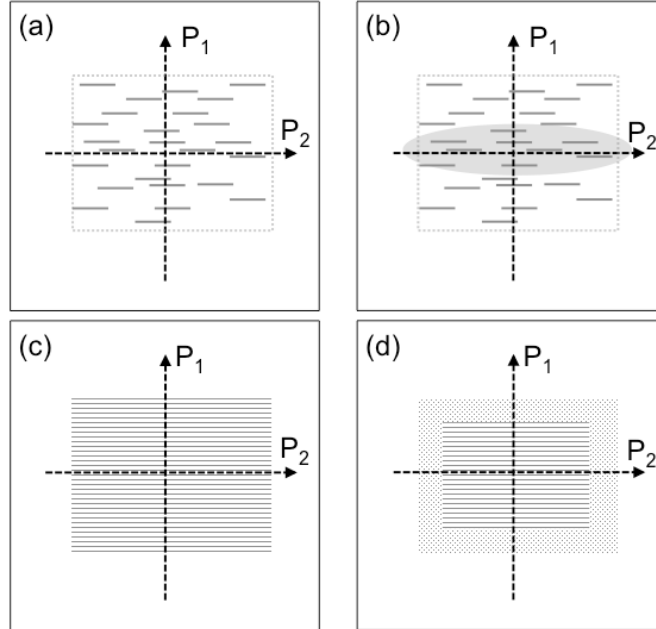
3

Figure 1: Schematic diagram of fracture induced seismic anisotropy: (a) two ray paths P_1 and P_2 (dashed arrows) travel through a fracture zone (within the dashed rectangle) with discrete fractures depicted by grey lines; (b) same as (a) but with the inclusion of a velocity anomaly (shaded ellipse); (c) same as (a) but with the discrete fracture zone represented by an effective homogeneous fracture zone; and (d) same as (c) but with the effective homogeneous fracture zone reduced in size and surrounded by a transition region (stippled region).

fine the transition region from scattering to anisotropy? How should we consider this transition in our quantitative estimates of fracture properties? To provide some insight into these fundamental questions, we study the development of SWS as a wave propagates through a fractured medium using the DFM approach. To do this, we model full-waveform seismic synthetics using the three-dimensional (3D) finite-difference (FD) algorithm WAVE (Hildyard, 2007) that models fracture networks as explicit discontinuity elements that can encapsulate individual fracture behaviour. By using the DFM approach we can explore the range of fracture properties that lead to effective anisotropy using heterogeneous yet coherent discontinuities by simulating the interaction of seismic waves with fractures. The DFM allows models to capture the influence of specific fracture properties, such as fracture size, stiffness and spacing (or density) on seismic SWS.

2. Methodology

In this section, we first describe the forward modelling approach and elastic models used to generate the FD full waveform seismic synthetics. Subsequently, we summarise the approach to calculate SWS with special attention to the evaluation of the SWS quality factor.

2.1. Numerical FD model

We use the full-waveform FD algorithm WAVE (Hildyard, 2007) to simulate wave propagation in 3D heterogeneous and isotropic media. The FD code computes the seismic wavefield on

4

equally-spaced, staggered orthogonal grid, where the variables stress and velocity are staggered at different points in time. The FD algorithm is second-order accurate in time and fourth-order accurate in space. Fractures are represented using the DFM approach, where each fracture or group of fractures are explicitly defined as a displacement discontinuity. The fracture surfaces have zero-thickness, where the difference in displacements across the two surfaces is related to the stress across the interface. The stress and discontinuity in displacement across the two surfaces are coupled by the fracture normal and tangential stiffnesses. In principal, the fracture stiffness accounts for the existence of asperities and voids between the surfaces of natural fractures (e.g., Baird et al., 2013; Petrovitch et al., 2013), leading to a finite coupling between the surfaces. Hildyard & Young (2002) benchmark WAVE and the DFM approach with laboratory experiments of ultrasonic wave propagation through natural fractures in rock (Pyrak-Nolte et al., 1990). Hildyard & Young (2002) show that the WAVE and the DFM approach accounts for frequency dependence of both the seismic velocity and the transmitted wave amplitude.
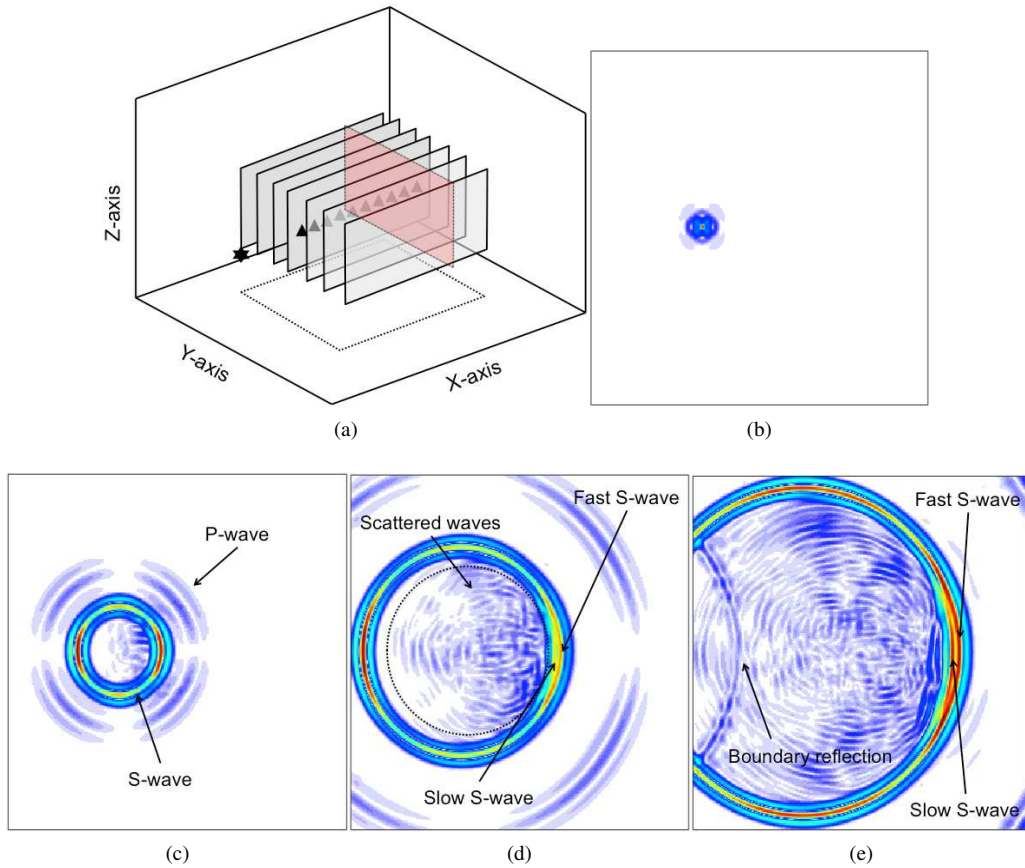

Figure 2: (a) Schematic view of the linear receiver array within the FD model. The star represents the source location, the triangles represent the receivers and the grey shaded rectangles represent the vertical and lateral extent of the discrete fracture zone. The red vertical plane depicts an example plane where we perform horizontal scans through the fracture volume to compute fracture spacing distribution. Snapshot of a seismic wave propagating in the x-y plane through a fractured medium for a double-couple source at time (b) t=7.9 ms, (c) t= 17.34 ms, (d) t=33.1 ms and (e) t=48.9 ms. In (d) the scattered waves are highlighted by the region within the dashed ellipse.

We consider a base fracture model having vertical fractures oriented along the x-axis within an isotropic background medium. The isotropic elastic medium has density $\rho = 2600$ kg/m^3, P-wave velocity $V_P = 5700$ m/s and S-wave velocity $V_S = 3200$ m/s ($V_P/V_S = 1.78$). The geometry of the model has overall dimension of $(x, y, z) = (300$ m, 300 m, 300 m). Seismic waves are generated using a moment tensor source having a seismic moment magnitude of 1×10^{14} dyne cm and a strike-slip double-couple mechanism with strike 90°, dip of 90° and slip 45°. The source time function has a dominant source frequency of approximately 180 Hz, and so we use a grid spacing of $\Delta h = 1$ m and time increment of approximately $\Delta t = 0.08$ ms to maintain numerical stability and minimise grid dispersion for all fracture model realisations. The source is located at $(x_s, y_s, z_s) = (100$ m, 150 m, 140 m) outside the fracture volume having dimension $(x, y, z)=(80$ m, 80 m, 80 m). A single linear array of 10 three-component receivers is defined, oriented along the direction of maximum SWS (i.e., along the x-axis) and located through the fracture volume (see Figure 2).

We generated a suite of 48 model realisations by varying one of three explicit fracture properties (compliance ratio, fracture size and fracture density) while keeping the other two constant. We focus on compliance ratio as this parameter has been used as an indicator for fracture fluid fill as well as fracture geometry (e.g., Verdon & Wüstefeld, 2013). For compliance ratio, Z_N/Z_T, we consider values of 0.33, 0.60 and 1.00, which are consistent with the range of values observed from laboratory and field measurements (e.g., Angus et al., 2012; Verdon & Wüstefeld, 2013; Choi et al., 2014). For fracture size, d, we consider values of 6, 10, 20 and 50 m for several reasons and constrained by the dominant wavelength ($\lambda_S \approx 18$ m) of the shear-wave. For crustal rock, the size (or height) of fractures ranges on the order of between 0.01 to 10 m (e.g., Narr, 2006; Barton, 2007). Thus the lower end values of 6 and 10 m represent typical values observed in the field yet having size that approaches the length scale of the dominant wavelength. Values above 10 m allow us to explore the transition from conditions where EMM would be valid to conditions where EMM for fractures would not be valid. Therefore the size range of the fractures allows us to examine the transition from LWA or Rayleigh scattering where $\lambda_S/d > 1$, to Mie scattering regime where $\lambda_S/d \rightarrow 1$, and to the high frequency or geometric scattering regime ($\lambda_S/d < 1$). For fracture density, ϵ, we used values of 0.02, 0.04, 0.08 and 0.10, which is consistent with field observations of naturally occurring fracture systems (e.g., Narr, 2006). The values of normal and tangential stiffnesses range on the order of between 1×10^9 to 1×10^{11} Pa/m. The specific values used are consistent with the laboratory and field-scale estimates of Worthington (2008) and Verdon & Wüstefeld (2013), and are dependent on the fracture size.

Figure 2 shows an example of shear-wave propagation through a fracture volume at 4 time steps to highlight the evolution of SWS, where the linear array allows us to monitor the evolution of the shear wavefront as it propagates through the fracture volume. (Note that the P-wave is barely visible because the x-y section is along the null axis of the P-wave radiation pattern of the double-couple source.) As the wave propagates, the right-hand side of the wavefront begins to interact with the fracture volume, where scattering can be observed behind the primary shear-wave. At later times, SWS can be observed on the right-hand side of the wavefront as well as significant scattering in the wavefield persisting behind the primary shear-wave within the fracture volume. The scattering that is observed is due to a combination of first-order (i.e., single) and higher-order (i.e., multiple) diffractions from fracture tips and edges as well as specular reverberations (i.e., multiply reflected energy) from fracture surfaces.

2.2. SWS methodology

We use the algorithm SHEBA (e.g., Teanby et al., 2004b; Wüstefeld et al., 2010) to compute the SWS parameters. The analysis of SWS requires first rotating the three component waveforms into a local ray coordinate frame, where the P-wave energy will be constrained to the ray direction (P) and the shear-wave energy on the two remaining components (S_V and S_H). The rotation can be done either using a standard rotation algorithm based on the polarisation filter approach of Montalbetti & Kanasewich (1970) or by assuming a straight ray path between the source and receiver. We compared both approaches and found very little difference in the respective local coordinate frames for our models, and so used the straight ray path approximation to reduce processing time. After rotation into the ray coordinate, an analysis window is specified relative to the shear-wave first arrival. Typically one window size is chosen but a range of window start and end times are evaluated to cover the maximum possible time delays that could be expected. A grid search of analysis windows over these intervals allows for a much faster calculation of SWS parameters than manual picking and provides a measure of the overall SWS quality Q (Wüstefeld et al., 2010).

Within the algorithm the time delay between the fast and slow shear-waves and the rotation angle for maximum splitting are calculated by two methods and compared to give a measure of quality. The first method is based on an eigenvalue method of Silver & Chan (1991), which takes into account the fact that if anisotropy is present then the particle motion within the window should be elliptical. The method uses a grid search over rotation angles and time difference. The second method is based on a cross correlation scheme (Teanby et al., 2004b). The rotated waveforms are correlated using the same windows, where the time lag associated with the largest correlation peak gives a measure the SWS time difference. By comparing the similarity in the calculated time differences from the two methods a Q_{SWS} value is defined, where values close to one represent good splitting and values close to negative one are good nulls (i.e., no SWS) (Wüstefeld et al., 2010). When the value of Q_{SWS} is close to zero, the data quality of the splitting is poor or inconclusive. Typically, with noisy data, values between -0.5 and 0.5 are discarded from further analysis. In our models, poor values would be expected due to the diffraction type scattering effects (e.g., Klem-Musatov et al, 2008) from the edge of the discrete fractures.

Figure 3 shows the results for a good splitting measurement, where an initial elliptical particle motion is linearised after an appropriate rotation and delay correction. The calculated delay time of 1.32 ms and fast polarisation direction of 36° is well constrained in both methods yielding Q_{SWS} = 0.96. Figure 3 also shows the result of a null splitting example, where the initial polarisation is linear. Since there is no SWS, the solution is not well constrained yielding Q_{SWS} = −0.98. For all fracture models, we apply the same SWS analysis to all receiver recordings to compute the delay time and associated quality factor.

3. Results

For all 48 models, we calculate the SWS parameters for all 10 receivers within the fracture volume. In Figures 4-7, we show the computed delay time δt for each station as a function of propagation length within the volume normalised by the shear wavelength (distance/λ_S). The quality of δt is given by colour contours, with Q_{SWS} = 1 red, Q_{SWS} = 0 green and Q_{SWS} = −1 blue.

Figure 4 displays the SWS results for the fracture models having fracture size d = 6 m. For this model, the dominant wavelength of the shear-wave is 3 times greater than the size of the
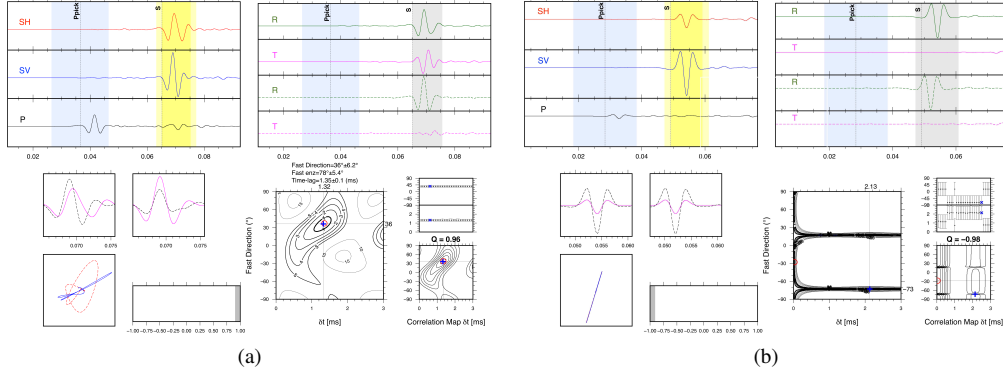
7

Figure 3: Example of (a) good SWS measurement ($Q = 0.96$) and (b) null splitting ($Q = -0.98$) for fracture model having size 6 m and $Z_N/Z_T = 0.33$. For (a) and (b); (top-left) 3 component waveforms in local ray coordinates; (top-right) radial and transverse components before (top 2 traces) and after (bottom 2 traces) splitting correction; (middle-left) fast (dashed) and slow (solid) S waves before (left) and after (right) correction; (bottom-left) particle motion in S_V-S_H coordinate frame before (dashed) and after (solid) correction; (bottom-right) error surfaces of the eigenvalue (left) and cross-correlation (lower right) methods (see Wüstefeld et al., 2010, for details). The best result of the two methods are shown as blue + and red circle for the eigenvalue and cross-correlation method, respectively; and (middle-right) fast axis (top) and δt variations for each window including corresponding error bars.

fractures such that the simulation results fall within the LWA regime (e.g., Ebrom et al., 1990; Marion et al., 1994). For all compliance ratios and fracture density, there is a general trend of spurious δt measurements for receivers located close to the source within approximately one wavelength of propagation distance. For these receivers the quality of the SWS measurements is low indicating either null or inconclusive measurements. For fracture density greater than 0.04 there is a general trend of increasing δt starting from a non-zero value (≈ 0.5 ms) up to approximately 3 ms with generally good SWS quality factors. For the lower fracture densities of 0.02 and 0.04, the quality of the SWS results are variable indicating that the model fracture density may not be of sufficient magnitude to induce shear-wave anisotropy. The results indicate that fracture density plays a more significant role on the evolution of SWS than compliance ratio.

Figure 5 displays the SWS results for the fracture models having fracture size $d = 10$ m. For fracture size $d = 10$ the model falls close to the border of the LWA regime, where the dominant shear wavelength is less than 2 times greater than the size of the fractures. As with Figure 4, there is a general trend of spurious low quality δt measurements within approximately one wavelength of propagation distance. For fracture density greater than 0.04 there is a general trend of increasing δt starting from a non-zero value (≈ 0.5 ms) up to approximately 2 ms with generally good SWS quality factors for receivers beyond 2 to 3 propagation wavelengths. For the lower fracture densities of 0.02 and 0.04, the quality of the SWS results are much more variable than those for fracture size $d = 6$ m indicating that the fracture size of $d = 10$ m leads to less reliable or coherent induce shear-wave anisotropy.

Figure 6 displays the SWS results for the fracture models having fracture size $d = 20$ m. The dominant shear wavelength has approximately the same order of magnitude of the fracture size such that the LWA is no longer valid and where we expect to observe Mie scattering. For all compliance ratios and fracture density the SWS results are unreliable and incoherent. In Figure 7, we show the results for fracture models having fracture size $d = 50$ m. The ratio of shear wavelength to fracture size falls in the high-frequency approximation (HFA) region, $\lambda/d \approx 2/5$
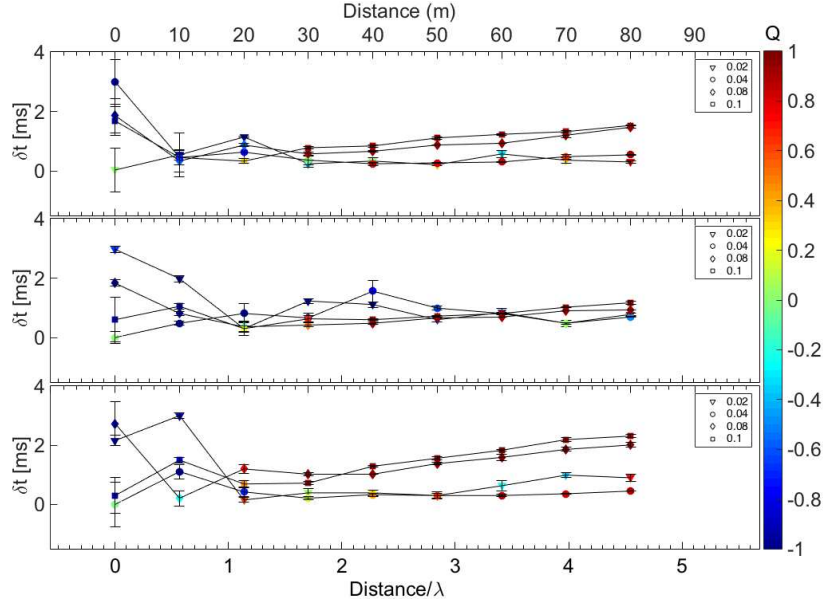
Figure 4: Evolution of SWS for fractures having size $d = 6$ m: (top) $Z_N/Z_T = 0.33$, (middle) $Z_N/Z_T = 0.60$ and (bottom) $Z_N/Z_T = 1.00$. The vertical axis represents the calculated delay time δt with corresponding error bars and the horizontal axis represents the propagation distance within the fracture volume normalised by the dominant wavelength $\lambda_S = 18$m. The colour contour of the symbols represents the quality factor of the SWS measurement. The fracture stiffness values are: ($Z_N/Z_T = 0.33$) $K_N = 6 \times 10^{10}$ Pa/m and $K_T = 2 \times 10^{10}$ Pa/m, ($Z_N/Z_T = 0.60$) $K_N = 5 \times 10^{10}$ Pa/m and $K_T = 3 \times 10^{10}$ Pa/m, and ($Z_N/Z_T = 1.00$) $K_N = 1 \times 10^{10}$ Pa/m and $K_T = 1 \times 10^{10}$ Pa/m. The legend in the top-right corner of each subplot represents the fracture density: inverted triangle=0.02, circle=0.04, diamond=0.08 and square=0.1

(e.g., Ebrom et al., 1990; Marion et al., 1994) where we expect to observe geometric scattering. As with the case of fracture size $d = 20$ m, the SWS results are incoherent with the exception of two models: $Z_N/Z_T = 0.60$ and $\epsilon = 0.1$, and $Z_N/Z_T = 1.00$ and $\epsilon = 0.08$. It is important to note that the fracture models used in WAVE are generated using random fracture assemblies given a range of fracture size and fracture density (Hildyard, 2007). For some of the random realisations the fracture distribution could form coherent and persistent planar features, similar to the influence of sedimentary layering that often leads to transverse isotropy (TI). Thus the interaction of the shear-wave with these large fractures could yield wave behaviour similar to that observed in TI media in the HFA regime. For larger fracture sizes or greater ray paths within the fracture volume, wave propagation would likely yield SWS having the same characteristics as that of horizontal TI media.

4. Implications

We have addressed the question of when fracture systems become seismically anisotropic, at least for the case of shear-waves. However, we have yet explored the implications of the transition zone between scattering and effective anisotropy. To do this, we compare our δt observations with predictions using the linear slip (LS) EMM representation of Schoenberg & Sayers (1995). The LS approach is used extensively in the seismological literature to transform fracture compliance
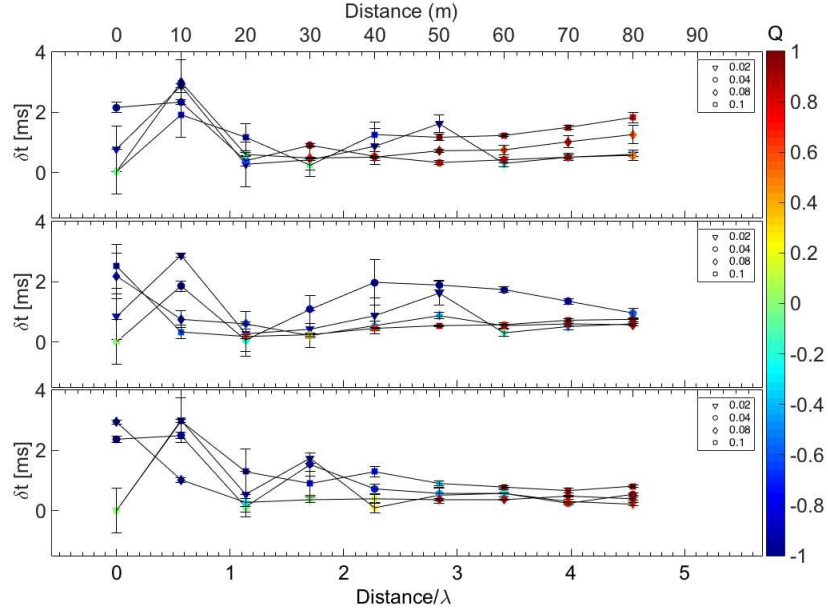
9

Figure 5: Evolution of SWS for fractures having size $d = 10$ m: (top) $Z_N/Z_T = 0.33$, (middle) $Z_N/Z_T = 0.60$ and (bottom) $Z_N/Z_T = 1.00$. The fracture stiffness values are: ($Z_N/Z_T = 0.33$) $K_N = 3 \times 10^{10}$ Pa/m and $K_T = 1 \times 10^{10}$ Pa/m, ($Z_N/Z_T = 0.60$) $K_N = 5 \times 10^{10}$ Pa/m and $K_T = 3 \times 10^{10}$ Pa/m, and ($Z_N/Z_T = 1.00$) $K_N = 3 \times 10^{10}$ Pa/m and $K_T = 3 \times 10^{10}$ Pa/m. See caption in Figure 4 for details.

to dynamic (i.e., seismic) elasticity, primarily because of to its generality (Hall, 2000) due to the fracture compliances being rotationally invariant (Barton, 2007).

First we compute the background stiffness matrix C_{ISO} based on the model density and isotropic P- and S-wave velocities. The background elasticity is then inverted to yield the background compliance S_{ISO}, where we can then add the excess compliance due to the presence of fractures using the approach of Schoenberg & Sayers (1995). The excess compliance matrix (ΔS) of the fractured medium requires first converting the WAVE model specific compliances B_N and B_T (units Pa^{-1}) to effective compliances Z_N and Z_T (units mPa^{-1}) using

$$Z_i = f B_i, \tag{1}$$

where $i = N$ or T and f is the fracture spacing. The excess compliance matrix is given by

$$\Delta S = \begin{pmatrix} Z_N & 0 & 0 & 0 & 0 & 0 \\ 0 & 0 & 0 & 0 & 0 & 0 \\ 0 & 0 & 0 & 0 & 0 & 0 \\ 0 & 0 & 0 & 0 & 0 & 0 \\ 0 & 0 & 0 & 0 & Z_T & 0 \\ 0 & 0 & 0 & 0 & 0 & Z_T \end{pmatrix}. \tag{2}$$

The excess compliance matrix is normalised by the cell size (Δh)
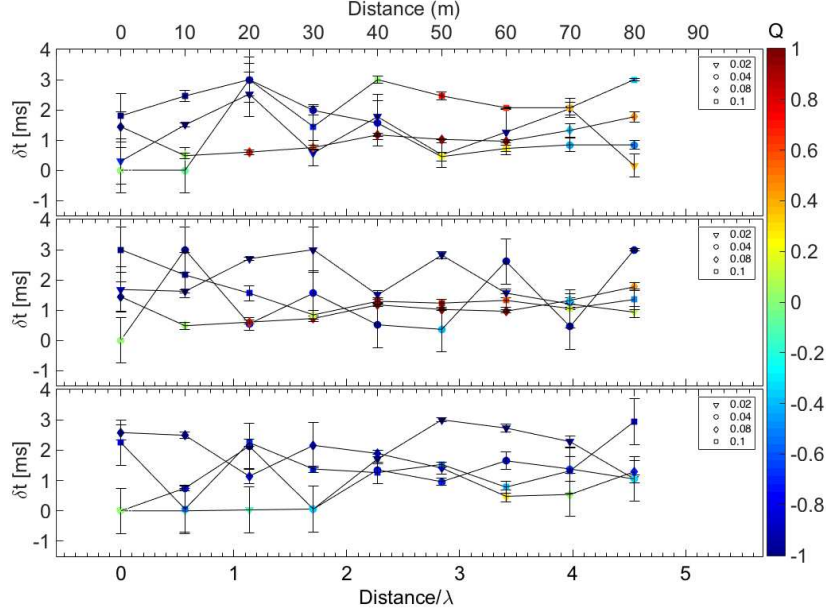
$$\Delta \bar{S} = \Delta S / \Delta h. \tag{3}$$

10

Figure 6: Evolution of SWS for fractures having size $d = 20$ m: (top) $Z_N/Z_T = 0.33$, (middle) $Z_N/Z_T = 0.60$ and (bottom) $Z_N/Z_T = 1.00$. The fracture stiffness values are: ($Z_N/Z_T = 0.33$) $K_N = 3 \times 10^9$ Pa/m and $K_T = 1 \times 10^9$ Pa/m, ($Z_N/Z_T = 0.60$) $K_N = 5 \times 10^9$ Pa/m and $K_T = 3 \times 10^9$ Pa/m, and ($Z_N/Z_T = 1.00$) $K_N = 1 \times 10^9$ Pa/m and $K_T = 1 \times 10^9$ Pa/m. See caption in Figure 4 for details.

Finally, the overall compliance is given by

$$S = S_{ISO} + \Delta\bar{S} \tag{4}$$

and then inverted to yield the LS effective elastic stiffness tensor C_{EMM}.

The approach we use to compute the fracture spacing follows that of Borgos et al. (2000) and Worthington (2008). For each grid point along the ray path from the source to the receivers through the fracture volume, we define a vertical plane having dimension 36×36 m^2 (approximately the dimension of the first two Fresnel zones for a transmitted wave, e.g., see Figure 2a). Within the plane we compute the distribution of fracture spacing using horizontal scan lines within the plane, each line separated vertically by the FD grid spacing Δh. Figure 8 shows the fracture spacing distribution for each vertical plane in the whole fracture volume as well as within the first two Fresnel zones, where the general trend shows a right (positive) skewed distribution with peak fracture spacing between 2 and 3 m. Summing the distribution for all vertical plane we get an approximate distribution of the fracture spacing: 4% for 1 m spacing, 32% for 2 m spacing, 37% for 3 m spacing, 19% for 4 m spacing, and 5% for 5 m spacing.

Figure 9 compares the measured SWS results for the fracture model having $d = 6$ m, $\epsilon = 0.1$ and $Z_N/Z_T = 0.33$ with several LS EMM predictions. For the simplest prediction we use an approximate average fracture spacing of 2.5 m and 6 m and observe that LS over predicts SWS. Next we compute the excess compliance based on the summed average fracture spacing distribution using 6 different means: arithmetic, geometric, harmonic, quadratic, cubic and weighted.
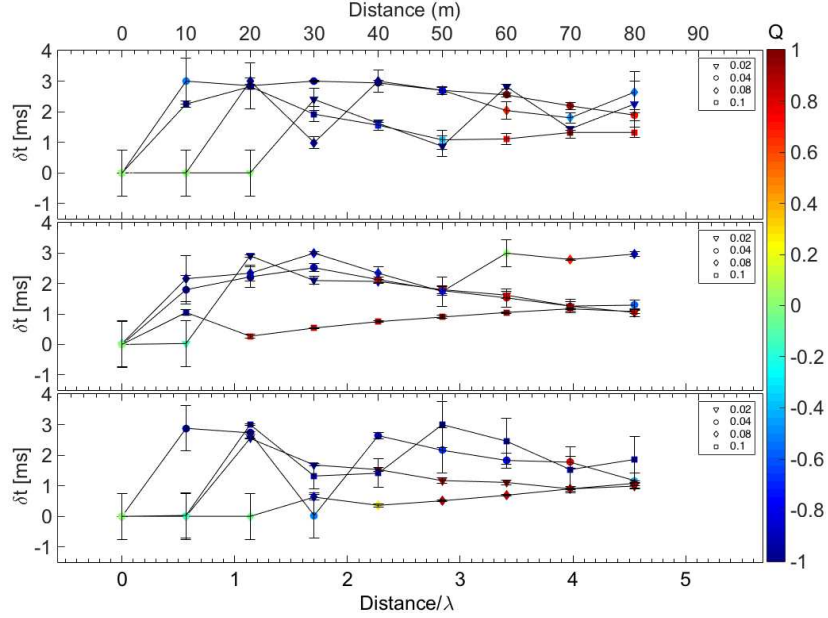
11

Figure 7: Evolution of SWS for fractures having size $d = 50$ m: (top) $Z_N/Z_T = 0.33$, (middle) $Z_N/Z_T = 0.60$ and (bottom) $Z_N/Z_T = 1.00$. The fracture stiffness values are: ($Z_N/Z_T = 0.33$) $K_N = 3 \times 10^9$ Pa/m and $K_T = 1 \times 10^9$ Pa/m, ($Z_N/Z_T = 0.60$) $K_N = 5 \times 10^9$ Pa/m and $K_T = 3 \times 10^9$ Pa/m, and ($Z_N/Z_T = 1.00$) $K_N = 3 \times 10^9$ Pa/m and $K_T = 3 \times 10^9$ Pa/m. See caption in Figure 4 for details.

For example, the weighted mean excess compliance is given

$$\Delta S = \frac{\sum_{i=1}^{5} w_i \Delta S_i}{\sum_{i=1}^{5} w_i}, \tag{5}$$

where w_i is the fractional distribution of the i-th fracture spacing (i.e., $w_1 = 0.04$) and ΔS_i is the corresponding compliance. As can be seen, most of the LS predictions do not match the observed SWS trend of the data and over predict the amount of shear-wave anisotropy. Only the weighted mean average comes close to predicting a broadly similar trend, yet under predicting the shear-wave anisotropy and having a shallower slope.

To estimate the LS EMM model parameters that would fit the data, we perform a grid search over one fracture parameter while keeping the other two constant. In the first case we assume *a priori* model fracture compliances of $Z_N = 1.7 \times 10^{-11}$ m/Pa and $Z_T = 5 \times 10^{-11}$ m/Pa (i.e., exact values from FD model) that might be available from laboratory core measurements. The best fit LS model requires a fracture spacing of 10 m. In the second case we assume *a priori* an average model fracture spacing of 2.5 m (i.e., approximate mode value for the summed distribution) and compliance ratio of $Z_N/Z_T = 0.33$ that might be available from laboratory core measurements. The best fit LS model requires fracture normal and tangential compliances of $Z_N = 2.7 \times 10^{-11}$ m/Pa and $Z_T = 8.2 \times 10^{-11}$ m/Pa, respectively. Based on these two cases, the error from using the LS EMM prediction would lead to a 400% error in fracture spacing and 60% error in fracture compliance.

There are two important implications to the results: (1) any EMM will predict that anisotropy
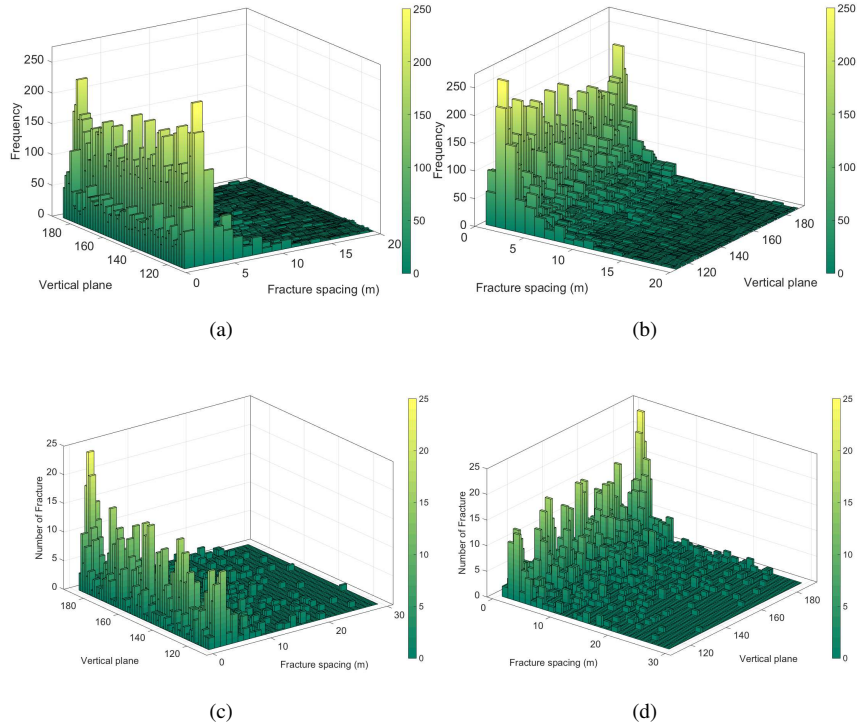
12

Figure 8: Histogram showing the distribution of fracture spacing for the whole volume (a and b) and that the shear-wave would be sensitive to as the wave propagates through the fracture volume (c and c) based on the first and second Fresnel zone. Perspective views shows (a and c) the distribution of the small fracture spacing and (b and d) the distribution of the larger spacing. Each vertical plane provides an estimate of the fracture spacing within the first two Fresnel zones $(2 \times \lambda_S \approx 36\text{m})$ tangential to the direction of wave propagation.

will develop instantaneously as the wave propagates through the model and neglects the influence of the transition zone and (2) the LS EMM significantly over predicts seismic anisotropy. The first observation suggests that EMM predictions from SWS measurements near the source will suffer from inaccuracies as seismic anisotropy will have very little time to develop. The strength of seismic anisotropy is coupled to the path length within the anisotropic volume (e.g., Savage, 1999). This is analogues to the slope (δt/distance) of the trends shown in Figure 9. As the distance of SWS observation moves further from the seismic source and the ray path within the zone exceeds 2 to 3 propagation wavelengths, EMM predictions will suffer less from the influence of the transition zone. This is because the slope of the best-fitting EMM prediction will approach asymptotically that of the observations (i.e., $f = 10$ m). For most observational applications it is not practical to acquire data with sensors within a fracture volume: for laboratory data this might require drilling a core through the middle of the sample to place sensors or placing sensors within a synthetic rock specimen during manufacturing whereas for field data this might require access to one or more boreholes that intersect a fracture volume where sensors could be position throughout the fractures system. This could be achieved on out-crop scale but would involve special processing of the seismic data to compensate for free surface effects.
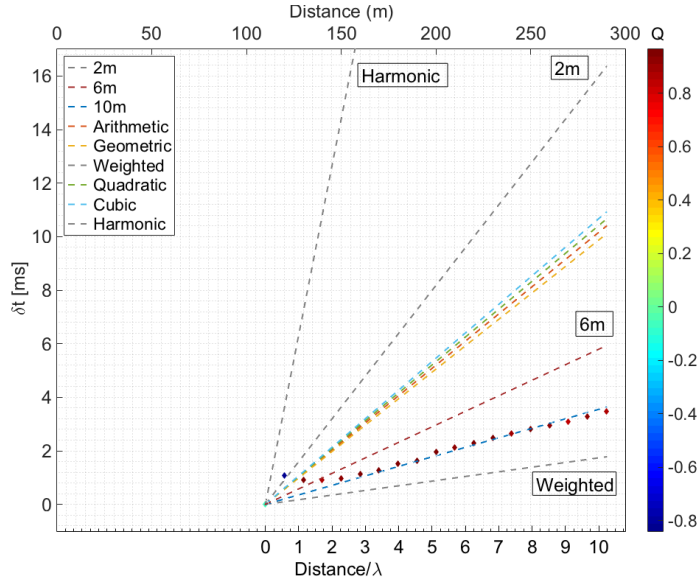
13

Figure 9: Comparison of LS EMM δt predictions with the observed SWS for the fracture model: $d = 6$ m, $\epsilon = 0.1$ and $Z_N/Z_T = 0.33$. LS EMM predictions of Schoenberg & Sayers (1995) for spacing 2 m, 6 m and 10 m (best fitting LS EMM model) as well as LS EMM predictions from the summed distribution in Figure 8 using 6 different means: arithmetic, geometric, harmonic, quadratic, cubic and weighted. See caption in Figure 4 for details.

The second observation is more concerning given that the LS model is used pervasively in the seismological community. Chichinina et al. (2015) analyse the limitations of Schoenberg & Sayers (1995) LS model and find that their model is not generally adequate for real rocks. Chichinina et al. (2015) note that the LS model is only valid for two conditions: (1) when $Z_N = 0$ (i.e., case of fluid-filled fractures) or (2) when the scalar crack $Z_N/Z_T = 1$ is assumed (i.e., Bakulin et al., 2000). Hildyard (2001) observed that the LS model was only accurate for high-stiffness fractures and became increasingly inaccurate as the stiffness decreased, which is consistent with the first condition $Z_N = 0$. Regarding the second condition $Z_N/Z_T = 1$, it has been observed from laboratory (e.g., MacBeth & Schuett, 2007; Angus et al., 2012; Choi et al., 2014) and field (e.g., Worthington, 2008; Verdon & Wüstefeld, 2013) data that the scalar crack assumption is not universally consistent. For the case of $d = 6$m, $\epsilon = 0.1$ and $Z_N/Z_T = 1.00$ we observe the same misfit of the LS predictions with the synthetic data (see Figure S1 in the supplemental material). Thus, even for the scalar crack case, our results indicate that the LS model is inconsistent with the vast majority of real fracture behaviour. This brings us to another important limitation of the LS model, the assumption that the lateral dimension of linear slip interface be greater than the dominant seismic wavelength (Hsu & Schoenberg, 1993) or the assumption of a smooth stress field (Kachanov, 1992) thus limiting scattering within the fracture normal direction. For our models, the wavelength of the S-waves range on the order of the fracture size (i.e., the fracture size is not significantly greater than the wavelength) and so the LS model does not model the scattering from fracture edges and tips

It should be noted that the general assumption involved with the LS model is the LWA, such that $\lambda_S/d \gg 1$ (Sayers & Kachanov, 1991; Schoenberg & Sayers, 1995). In our simulations, the

14

smallest fracture size is $d = 6$ m, which lies on the boundary of where the LWA is valid (i.e., $\lambda_S/d \approx 3$). To test LWA, we simulate a seismic source having dominant frequency of 50 Hz with a wavelength of approximately 65 m (i.e., $\lambda_S/d \approx 10$). Again, we observed that at least 1 to 2 propagation wavelengths is needed before SWS develops and, even under the appropriate LWA conditions, we observe the same misfit of the LS predictions with the synthetic data (see Figure S2 in the supplemental material).

Thus, based on our results, we suggest that if SWS is to be used to quantify fracture properties the following criteria should be met:

1. Ray paths through the fracture volume should exceed 2 wavelengths to detect anisotropy and be at least 5 wavelengths to minimise the influence of the transition for quantitative estimates,
2. The ratio of dominant wavelength to expected fracture size should be greater than or equal to 3, and
3. The LS model should not be used for quantitative estimates, unless there is further data to calibrate the EMM results to *in situ* properties.

The last point is salient since the inversion of seismic anisotropy for fracture properties is increasingly being used to populate and calibrate multi-physical models of the subsurface (e.g., Angus et al., 2015). Significant errors in fracture property estimates will lead to over or under predicting the multi-physical response, which can have significant impact on hazard assessment and risk mitigation.

5. Conclusions

We have shown the scale-dependence of seismic anisotropy with new results specific to SWS. We explored the influence of Rayleigh, Mie and geometric scattering on shear-wave propagation through explicit fracture volumes. We find that SWS develops under conditions when the ratio of wavelength to fracture size is greater than 3 (Rayleigh scattering), where scattering from coherent fractures leads to an effective anisotropy. When the ratio of wavelength to fracture size is between 1 and 3, the scattering regime transitions from Rayleigh to Mie and no effective anisotropy develops. Within the Mie scattering regime the SWS measurements are unstable and of poor quality. When wavelength to fracture size is less than 1, geometric scattering occurs and we potentially observe behaviour similar to transverse isotropy. In terms of fracture properties, we observe that seismic anisotropy is more sensitive to fracture density than fracture compliance ratio. We observe that the transition from scattering to an effective anisotropic regime occurs over a propagation distance between 1 to 2 wavelengths and as such indicates that the inversion of seismic anisotropy parameters based on EMM will be biased. More importantly, we find that the linear slip effective medium model is inconsistent with our results. We show that application of the linear slip model to predict fracture properties leads to errors of approximately 400% in fracture spacing (equivalent to fracture density) and 60% in fracture compliance.

It should be noted that numerous studies based on the linear slip EMM representation have yielded reliable estimates fracture orientation and the spatial location of fracture systems. However, our results indicate that the linear slip model will systematically fail in providing quantitatively accurate estimates of physical fracture properties, such as fracture density and compliance. EMM approaches are still valuable, especially in terms of identifying the location and orientation of fracture sets as well as semi-quantitatively estimates of temporal variations in fracture properties, such as compliance ratio. For accurate and robust quantitative estimates of *in situ* fracture

properties, improvements to effective medium models will be required as well as the incorporation of a full-waveform inversion techniques that enable capturing the influence of stress state as well as specific fracture properties such as fracture size, filling and compliance.

Acknowledgements

References

Angus, D.A., Dutko, M., Kristiansen, T.G., Fisher, Q.J., Kendall, J-M., Baird, A.F., Verdon, J.P., Barkved, O.I., Yu, J. & Zhao, S. (2015) Integrated hydro-mechanical and seismic modelling of the Valhall reservoir: A case study of predicting subsidence, AVOA and microseismicity, *Geomechanics for Energy and the Environment*, **2**, 32-44.

Angus, D.A., Fisher, Q.J. & Verdon, J.P. (2012) Exploring trends in microcrack properties of sedimentary rocks: An audit of dry and water saturated sandstone core velocity-stress measurements, *Int J Geosc*, **3**, 822-833.

Babuska, V. & Cara, M. (1991) *Seismic anisotropy in the Earth*, Springer Science & Business Media, **10**, p. 217.

Baird, A.F., Kendall, J-M. & Angus, D.A. (2013) Frequency dependent seismic anisotropy due to fracture: Fluid flow versus scattering, *Geophysics*, **78** (2), WA111-WA122.

Bakulin, A., Grechka, V. & Tsvankin, I. (2000) Estimation of fracture parameters from reflection seismic data - Part I: HTI model due to a single fracture set, *Geophysics*, **65**(6), 1788-1802.

Barton, N. (2007) *Rock Quality, Seismic Velocity, Attenuation and Anisotropy*, Taylor & Francis, UK. p.729.

Borgos, H.G., Cowie, P.A. & Dawers, N.H. (2000) Practicalities of extrapolating one-dimensional fault and fracture size-frequency distributions to higher-dimensional samples, *Journal of Geophysical Research*, **105**, 28377-28391.

Chichinina, T., Obolentseva, I. & Dugarov, G. (2015) Effective-medium anisotropic models of fractured rocks of TI symmetry: Analysis of constraints and limitations in linear slip model, *SEG New Orleans Annual Meeting Expanded Abstracts*, 421-426.

Choi, M.K., Pyrak-Nolte, L.J. & Bobet, A. (2014) The effect of surface roughness and mixed-mode loading on the stiffness ratio K_x/K_z for fractures, *Geophysics*, **79**(5), D319-D331.

Cook, P.J. *Geologically storing carbon: Learning from the Otway Project Experience*, editor Cook, P.J., Australia: CSIRO Publishing, p. 384.

Cornet, F.H. (2015) *Elements of Crustal Geomechanics*, Cambridge University Press, p.461.

Crampin, S. (1981) A review of wave motion in anisotropic and cracked elastic- media, *Wave Motion*, **3**, 343-391.

Crampin, S. (2005) A review of shear-wave splitting in the compliant crack-critical anisotropic Earth, *Wave Motion*, **41** (1), 59-77.

Ebrom, D., Tatham, R., Sekharan, K.K., McDonald, J.A. & Gardner, G.H.F. (1990) Dispersion and anisotropy in laminated versus fractured media: an experimental comparison, *SEG Expanded Abstracts*, SN2.4, 1416-1419.

Fisher, Q.J., Casey, M., Harris, S.D. & Knipe, R.J. (2003) Fluid-flow properties of faults in sandstone: The importance of temperature history, *Geology*, **31**, 965-968.

Franciss, F.O. (2010) *Fractured Rock Hydraulics*, CRC Press, p.179.

Gaucher, E., Schoenball, M., Heidbach, O., Zang, A., Fokker, P.A., van Wees, J-D. & Kohl, T. (2015) Induced seismicity in geothermal reservoirs: A review of forecasting approaches, *Renewable and Suistainable Energy Reviews*, **52**, 1473-1490.

Hall, S. (2000) *Rock fracture characterisation and seismic anisotropy: Application to ocean bottom seismic data*, PhD thesis, University of Leeds, p. 195.

Hamlyn J.E., Keir, D., Wright, T.J., Neuberg, J.W., Goitom, B., Hammond, J.O.S., Pagli, C., Oppenheimer, C., Kendall, J.M. & Grandin, R. (2014) Seismicity and subsidence following the 2011 Nabro eruption, Eritrea: Insights into the plumbing system of an off-rift volcano, *Journal of Geophysical Research B: Solid Earth*, **119**, pp.8267-8282.

Hammond, J.O.S., Kendall, J-M., Angus, D.A. & Wookey, J. (2010) Interpreting spatial variations in anisotropy: insights into the Main Ethiopian Rift from SKS waveform modelling, *Geophysical Journal International*, **181**, pp.1701-1712.

Herwanger, J. & Koutsabeloulis, N. (2011) *Seismic Geomechanics: How to Build and Calibrate Geomechanical Models Using 3D and 4D Seismic Data*, EAGE.

Hildyard, MW (2001) *Wave Interaction with Underground Openings in Fractured Rock*, PhD thesis, University of Liverpool, p. 283.

Hildyard, M.W. (2007) Manuel Rocha Medal Recipient - Wave interaction with underground openings in fractured rock, *Rock Mech Rock Eng*, **40**, 531-561.

Hildyard, M.W. & Young, R.P. (2002) Modelling seismic waves around underground openings in fractured rock, *Pure Appl Geophys*, **159**, 247-276.

Hsu, C.J. & Schoenberg, M. (1993) Elastic waves through a simulated fractured medium, *Geophysics*, **58**(7), 964-977.

Jaeger, J., Cook, N. & Zimmerman, R. (2007) *Fundamentals of Rock Mechanics*, 4th edition, John Wiley and Sons, p. 470.

Jones, I.F. (2010) *An introduction to: velocity model building*, EAGE publications, p. 295.

Kachanov, M. (1992) Effective elastic properties of cracked solids: critical review of some basic concepts, *Appl. Mech. Rev.*, **45**(8), 304-334.

Keir, D., Belachew, M., Ebinger, C.J., Kendall, J.M., Hammond, J.O.S., Stuart, G.W., Ayele, A. & Rowland, J.V. (2011) Mapping the evolving strain field during continental breakup from crustal anisotropy in the Afar Depression, *Nature Communications*, **2**(1), 285.

Klem-Musatov, K., Aizenberg, A., Pajchel, J. & Helle, H.B. (2008) *Edge and tip diffractions: theory and applications in seismic prospecting*, Geophysical Monograph Series **14**, Society of Exploration Geophysicists, p. 210.

Liu, E.R. & Martinez, A. (2012) *Seismic Fracture Characterization: Concepts and Practical Applications*, EAGE.

MacBeth, C. & Schuett, H. (2007), The stress dependent elastic properties of thermally induced microfractures in aeolian Rotliegend sandstone, *Geophysical Prospecting*, **55** (3), 323-332.

Marion, D., Mukerji, T. & Mavko, G. (1994) Scale effects on velocity dispersion: from ray to effective medium theories in stratified media, *Geophysics*, **59**(10), 1613-1619.

Maultzsch, S., Chapman, M., Liu, E. & Li, X.Y. (2003) Modelling frequency-dependent seismic anisotropy in fluid-saturated rock with aligned fractures: implication of fracture size estimation from anisotropic measurements, *Geophys Pros*, textbook51(5), 381-392.

Montalbetti, J.M., & Kanasewich, E.R. (1970) Enhancement of teleseismic body phases with a polarization filter, *Geophys. J. R. astr. Soc.*, **21**, 119-129.

Narr, W. (2006) *Naturally Fractured Reservoir Characterization*, Society of Petroleum Engineers.

Nakagawa, S., Nihei, K.T., Myer, L.R. & Majer, E.L. (2003) Three-dimensional elastic wave scattering by a layer containing vertical periodic fractures, *J. Acoust. Soc. Am.*, **113**, 3012-3023.

O'Connell, R.J. & Budiansky, B. (1974) Seismic velocities in dry and saturated cracked solids, *J. Geophys. Res.*, **79**, 5412-5426.

Petrovitch, C., Pyrak-Nolte, L.J. & Nolte, D.D. (2013) Scaling of fluid flow versus fracture stiffness, *Geophysical Research Letters*, **40**(10), 2076-2080.

Pyrak-Nolte, L.J., Myer, L.R. & Cook, N.G.W. (1990) Anisotropy in seismic velocities and amplitudes from multiple parallel fractures, *J. Geophys. Res.*, **95**(B7), 11345-11358.

Rolandone, F., Bürgmann, R. & Nadeau, R.M. (2002) Time-dependent depth distribution of aftershocks: implications for fault mechanics and crustal rheology, *Seism. Res. Lett.*, **73**, 229, 2002.

Savage, M.K. (1999) Seismic anisotropy and mantle deformation: What have we learned from shear wave splitting, *Reviews of Geophysics*, **37**, 69-106.

Sayers, C.M. & Kachanov, M. (1991) A simple technique for finding effective elastic-constants of cracked solids for arbitrary crack orientation statistics, *Int. J. Solids Structures*, **27**(6), 671-680.

Schoenberg, M. & Sayers, C.M. (1995) Seismic anisotropy of fractured rock, *Geophysics*, **60**, 204-211.

Segall, P. (2010) *Earthquake and volcano deformation*, Princeton University Press, p. 432.

Silver, P.G. & Chan, W.W.J. (1991) Shear-wave splitting and subcontinental mantle deformation, *Journal of Geophysical Research*, **96**, 16429-16454.

Teanby, N.A., Kendall, J-M., Jones, R.H. & Barkved, O.I. (2004a) Stress-induced temporal variations in seismic anisotropy observed in microseismic data, *Geophysical Journal International*, **156**, 459-466.

Teanby, N.A., Kendall, J-M. & van der Baan, M. (2004b) Automation of shear-wave splitting measurements using cluster analysis, *Bulletin of the Seismological Society of America*, **94**(2), 453-463.

Verdon, J.P., Angus, D.A., Kendall, J.M. & Hall, S.A. (2008) The effect of microstructure and nonlinear stress on anisotropic seismic velocities, *Geophysics*, **73**, D41-D51.

Verdon, J.P. & Wüstefeld, A. (2013) Measurement of the normal/tangential compliance ratio (ZN/ZT) during hydraulic fracture stimulation using shear wave splitting data, *Geophys Pros*, **61**, 461-475.

Worthington, M. (2008) Interpreting seismic anisotropy in fractured reservoirs, *First Break*, **26**, 57-63.

Wüstefeld A., Al-Harrasi O., Verdon J.P., Wookey J. and Kendall J.-M. (2010) A strategy for automated analysis of passive microseismic data to study seismic anisotropy and fracture characteristics, *Geophysical Prospecting*, **58**, 755-773.

Yi, W., Nihei, K.T., Rector, J.W., Nakagawa, S., Myer, L.R. & Cook, N.G.W. (1997) Frequency-dependent seismic

anisotropy in fractured rock, *Int. J. Rock Mech. & Min. Sci.*, **34**(3-4), 349.

Zoback, M.D. & Gorelick, S.M. (2012) Earthquake triggering and large-scale geologic storage of carbon dioxide, *Proceedings of the National Academy of Sciences*, **109**(26), 10164-10168.